Science Advances

AAAS

advances.sciencemag.org/cgi/content/full/1/9/e1500682/DC1

Supplementary Materials for

Past and future rainfall in the Horn of Africa

Jessica E. Tierney, Caroline C. Ummenhofer, Peter B. deMenocal

Published 9 October 2015, *Sci. Adv.* **1**, e1500682 (2015)
DOI: 10.1126/sciadv.1500682

The PDF file includes:

Supplementary Materials and Methods

1. Core sites & chronology

We use a marine sediment box core (P178-15 BC1) to reconstruct recent climate trends (ca. AD 1600–present), and an accompanying piston core (P178-15 P) to extend the record back to ca. AD 100. These cores were collected from the Gulf of Aden at 11° 57.3' N, 44° 18' E, 869 meters water depth from the *R/V Pelagia* in 2001. The chronology of the box core (BC1) consists of a combination of ^{210}Pb dating on the top 16 cm of the core (Table S1) and 6 radiocarbon dates of *Globigerinoides ruber* (white) (Table S2). ^{210}Pb dating was achieved by gamma counting. We estimated background (supported) ^{210}Pb from the average of the measurements taken at 16.5 cm and 26.5 cm, which were identical within error (Table S1), and then subtracted that value from the rest of the measurements to calculate unsupported ^{210}Pb. A plot of depth versus $ln(^{210}\text{Pb})$ indicates a constant sedimentation rate, with the exception of an inversion between 3.25–5.5 cm (Fig. S1). The structure in this inversion suggests a diagenetic process affecting the ^{210}Pb concentration rather than mixing of the sediment, which would be expected to homogenize values. Thus, for calculation of sedimentation rates, we excluded the data at 3.25 cm, 3.75 cm, 4.75 cm, and 5.5 cm. We used a Monte Carlo procedure to propagate uncertainties related to the background ^{210}Pb assignment and the analytical errors associated with the ^{210}Pb measurements, and determined that the sedimentation rate for the top portion of the core was 0.18 ± 0.07 (2σ) cm/year. This ensemble of sedimentation rates was used to calculate ages at the measured depths along with propagated uncertainties (Table S1).

The radiocarbon dates on the lower portion of P178-15 BC1 imply a slower sedimentation rate of ca. 0.1 cm/year. As the probability of this sedimentation rate being compatible with the ^{210}Pb dates is 0.014, this indicates that some compression in the box core occurs with increasing depth and yields a slower sedimentation rate. To construct a combined ^{210}Pb and ^{14}C-based age model for the box core, we utilized the P_Sequence routine in OxCal 4.2 (*43, 44*). The combination of ^{210}Pb and ^{14}C dates in the OxCal framework also allows for a Bayesian determination of the marine reservoir correction (ΔR). Although there are independent observations of the ΔR in the Gulf of Aden, (*45, 46*) there is considerable uncertainty in these values, which range from 110–305 years. In OxCal, we set a relatively uninformative prior for ΔR of $300 \pm 100, 1\sigma$ and allowed the data to narrow the posterior value. OxCal's P_Sequence models sedimentation as a monotonic Poisson process (*44*) with a user-specified step size (k, an inverse value). We set k to 5, a relatively stiff value to represent the assumption that the sedimentation rate changes smoothly in this short box core. Figure S2 displays the results of this age modeling process. The posterior value for ΔR is considerably narrower than the prior, and this value ($311 \pm 24, 1\sigma$) was subsequently used in the age-depth model for the longer piston core (P178-15P).

Our previous work established a chronology for P178-15P extending back to ca. 40 ka based on

20 accelerated mass spectrometry (AMS) radiocarbon dates of *Globigerinoides ruber* (white) *(9)*. To improve the chronology for the Late Holocene section of the core, we analyzed an additional 12 dates (Table S3) using *Globigerinoides ruber* (white) and recalculated the age-depth model in OxCal. We used the ΔR value inferred from the box core and a k value of 0.5, a more flexible value that accommodates the changes in the sedimentation rate that occur throughout the length of the core (9.6 meters). As the ^{14}C date near the top of the core (5.5 cm) has a date (475 ^{14}C year) that once corrected for the global and local marine reservoir would suggest a "postbomb" (>1950 AD) age (Table S3), it was not explicitly calibrated but rather used to place a uniform prior on the coretop age of 1950–2001 AD (year of collection). Table S3 lists the median calibrated ages for the dated intervals and Figure S3 shows the resulting high-resolution age model spanning from 4,000 yr BP to present.

2. Organic geochemical analyses

2.1. Sampling and preparation

Core P178-15 BC1 was subsampled for analyses every 0.5 cm from 0–5 cm core depth, and every 1 cm until the end of the core (41 cm). Core P178-15P was subsampled for analyses every 0.5 cm from 0–5 cm core depth, and every 1 cm until 100 cm core depth. Wet sediments were freeze-dried, homogenized, and then approximately 12–18 grams were extracted using an accelerated solvent extractor (ASE) 350 at a temperature of 100°C and maximum pressure of 1500 psi. The resulting total lipid extracts (TLEs) were evaporated to dryness using N_2 gas then further purified using column chromatography. TLEs were first separated into neutral and acid fractions over LC-NH_2 gel using CH_2Cl_2:isopropanol (2:1) and 4% acetic acid in ethyl ether as the respective eluents. The acid fraction was then methylated (heated to 50°C, overnight) using acetyl chloride-acidified GC grade methanol of a known isotopic composition. The methylated fatty acids (fatty acid methyl esters; FAMEs) were further purified over silica gel using hexane and CH_2Cl_2 as respective eluents. The CH_2Cl_2 fraction, containing the FAMEs, was dried under N_2 gas and then redissolved in hexane for analysis by gas chromatography. The neutral fraction was further purified over silica gel using hexane, CH_2Cl_2, and methanol as eluents. The methanol fraction was dried under N_2 gas, redissolved in hexane:isopropanol (99:1), and filtered through a 0.2 micron PTFE filter in preparation for analysis by high-performance liquid chromatography (HPLC).

2.2. Analyses

The hydrogen isotopic composition of the FAMEs was measured via gas chromatography-pyrolysis-isotope ratio monitoring mass spectrometry (GC-IR-MS) using a Thermo Finnigan Delta V Plus mass spectrometer at Woods Hole Oceanographic Institution. H_2 gas calibrated to an authentic n-alkane standard (the "A5" mix, provided by Arndt Schimmelmann at Indiana

University) was used as a working reference for each analysis. In addition, an internal standard (*cis*-11-eicosenoic acid) was added to each sample after extraction but before purification, and the A5 mix was analyzed every 10 samples to monitor drift and correct for any offsets. Samples were run at least in duplicate and typically in triplicate. The standard error of repeat analyses (precision) was 2‰ or better. Accuracy, based on repeat analysis of the A5 Mix, is 5‰.

We applied a mass balance correction for the addition of the methyl group during the methylation, as follows:

$$\delta D_{sample} = \frac{62 \times \delta D_{measured} - 3 \times \delta D_{meoh}}{59} \quad (1)$$

Where δD_{meoh} was determined to be -169±1‰ by repeat measurements of a phthalic acid standard of a known isotopic composition (provided by Arndt Schimmelmann at Indiana University) methylated with the same methanol used for the methylation of the target compounds.

We focused on analyzing the fatty acids, as opposed to the *n*-alkanes, in the Gulf of Aden sediments because they were more abundant and easier to purify for GC-IR-MS measurements. The fatty acids from P178-15P show peak abundance at chain lengths of 26 carbons (Fig. S4), but we measure the C_{30} fatty acid as the representative terrestrial leaf wax due to evidence that fatty acids of shorter chain lengths could potentially have a competing aquatic origin in the marine environment (*47*). This is also the same chain length that we previously analyzed in P178-15P to construct a lower resolution record spanning back to 40,000 yr BP *(9)*. Low abundances precluded collecting C_{32} fatty acid data for comparison.

The filtered methanol fractions were analyzed for glycerol dialkyl glycerol tetraether (GDGT) distributions on an Agilent 1260 Infinity HPLC coupled to an Agilent 6120 single quadrupole mass spectrometer at Woods Hole Oceanographic Institution. Separation was achieved on a Grace Prevail Cyano column (2.1 x 150 mm, 3 μm) using the method of (*48*). TEX_{86} values were calculated from the peak areas of the respective GDGTs:

$$TEX_{86} = \frac{GDGT-2 + GDGT-3 + GDGT-5'}{GDGT-1 + GDGT-2 + GDGT-3 + GDGT-5'} \quad (2)$$

All samples were run in duplicate and repeat analyses had a standard error of 0.002 TEX_{86} units or better.

2.3. TEX_{86} calibration and interpretation

We calibrated our measured TEX_{86} values to sea-surface temperatures using BAYSPAR, a Bayesian calibration for the proxy that uses a global core top dataset to estimate errors *(10)*.

We specifically used the "BAYSPAR-NRS" version of the calibration, which omits coretop data from the Red Sea. The Red Sea TEX_{86} data are substantially different from the coretops in the Gulf of Aden and the Arabian Sea, possibly due to an influence of salinity or different producers in the enclosed basin (*49*). Their close proximity to our Gulf of Aden site means that their values heavily influence estimated mean annual temperatures when using the standard BAYSPAR calibration (via the spatial sharing parameter ϕ), even though they are not representative of local TEX_{86} distributions (BAYSPAR currently does not allow for the implementation of strict geographic boundaries to limit the influence of nearby data). The NRS calibration resolves the issue by omitting the Red Sea data. The prediction of SST therefore relies on coretops in the Gulf of Aden, Arabian Sea, and greater western Indian Ocean region and results in a better estimation of mean annual values.

As the BAYSPAR calibration employs a global estimation of error variance, the uncertainties surrounding calibration to absolute SSTs are large. However, the analytical precision of the TEX_{86} measurements translates to ca. 0.3°C; therefore, the proxy can capture small relative changes in temperature that characterize the Gulf of Aden during the past two millennia.

TEX_{86} is based on the relative cyclization of GDGTs produced by marine archaea. GDGTs are relatively refractory compounds, and the TEX_{86} index is not altered by diagenetic processes (*50*). The producers are presumed to be primarily epipelagic and mesopelagic Thaumarchaeota but may also include Euryarchaeota (*51*). Mesocosm experiments demonstrate that a mixed community of marine archaea systematically increase the TEX_{86} value of their lipids in response to increasing water temperatures (*52, 53*) and validates the use of TEX_{86} to infer water temperatures in the marine environment. The calibration of TEX_{86} to specifically SSTs is, however, empirical, and marine archaea producing GDGTs are known to inhabit both the epipelagic and mesopelagic zones (*54, 55*). TEX_{86} may therefore reflect integrated upper ocean temperatures rather than strictly SST, and in some locations may be more sensitive to subsurface (e.g., 100 meter) temperatures (*56*). On the timescales relevant to this study, we expect subsurface temperatures have largely tracked SSTs such that TEX_{86} may be used to infer SSTs reliably. Comparison between the box core TEX_{86}-derived SSTs and instrumental records of SST demonstrates that this is a valid assumption, as the magnitude of SST change reconstructed from TEX_{86} closely matches the observations (Fig. S5).

2.4. Leaf wax interpretation

The leaf waxes in our Gulf of Aden sediments likely arrive from the Horn of Africa via aeolian transport. Dust flux to the Gulf is seasonal, occurring predominantly in the dry months of June-August when the winds associated with the Indian summer monsoon sweep across the Horn (see ref. 9). The lack of dust transport during the winter months, when the winds are reversed, suggests that the Arabian Peninsula is not a major source region. Previous analyses of

pollen and radiogenic isotopes are consistent with the vegetation and lithology of easternmost Ethiopia, the Afar Triangle, and the eastern Horn of Africa region (*57–59*), and the carbon isotopic composition of the leaf waxes (ca. -24‰, see Fig. 2 and discussion below) are indicative of arid, C4-dominated vegetation. Hence, the leaf waxes likely derive from vegetation across the arid Horn, as opposed to vegetation from the more humid Ethiopian highlands or the Saudi Arabian peninsula.

Multiple studies demonstrate that δD_{wax} is a reliable proxy for δD_P across many different biomes (*60–62*) and previous work in the Gulf of Aden *(9)* and elsewhere in tropical Africa *(12,13,16)* suggests that δD_{wax} can be interpreted in terms of regional aridity. However, different types of plants (e.g., grass vs. tree) have slightly different "apparent" hydrogen isotopic fractionations (ε, i.e., the observed difference between δD_P and δD_{wax}) (*62*). If these differences in apparent ε are related to physiological differences between plants, then changes in the vegetation type from which the waxes derive over time could influence the δD_{wax} signature independently of climatic change. To assess whether vegetation changed substantially over the timescales relevant to our study we measured the carbon isotopic composition of the leaf waxes ($\delta^{13}C_{wax}$) which reflects the metabolic pathway of the source plants (e.g., C_3 vs. C_4, each associated with distinctive carbon isotopic fractionations) (*63*) and in tropical Africa is a reliable indicator for different landscape types (*64–66*). These data show very little variation during the past millennium aside from a recent depletion trend (Fig. 2). This recent depletion in $\delta^{13}C_{wax}$ can be attributed to the Suess effect, as it resembles the record of atmospheric CO_2 $\delta^{13}C$ both in timing and in magnitude (Fig. 2). These $\delta^{13}C_{wax}$ data, along with previously-collected data from P178-15P that indicate $\delta^{13}C_{wax}$ has varied by less then 1‰ in the last 4,000 years *(9)*, suggest that vegetation cover in the Horn of Africa region has not changed substantially over the timescales of this study and that δD_{wax} may be interpreted straightforwardly as a proxy for aridity. Furthermore, the detection of the Suess effect in the $\delta^{13}C_{wax}$ data suggests that the leaf waxes reaching the core site in the Gulf of Aden are not substantially pre-aged.

The δD_{wax} data indicate a rapid increase in aridity during the 20^{th} century (Fig. 1). To assess how unusual this rise is, we resampled the δD_{wax} to an even time interval (10 years), applied a 10-pt (100-yr) Gaussian smoothing filter to the data to isolate century-scale variability, and then took the first derivative. The rate of change in δD_{wax} in the 20^{th} century, especially in the box core data, is much greater than rates seen in the last 2,000 years, and has been consistently positive since the early 1800s (Fig. S6).

3. General circulation model analyses

3.1. CMIP5 models & experiments

We used climate model output from the Coupled Model Intercomparison Project 5 (CMIP5) experiments, including data from the "historical" experiment and the Representative Concentration Pathway (RCP 8.5) experiment. The data are publicly available online via the Earth System Grid: `http://pcmdi9.llnl.gov/`. The historical experiment simulates climate changes from 1850–2005 with the full range of observed forcings (solar, volcanic, orbital, greenhouse gas, aerosols, and land use data). The RCP 8.5 scenario simulates climate from 2006–2100, and involves continuously raising greenhouse gas emissions such that the radiative forcing reaches 8.5 W/m^2 by year 2100 (*67, 68*). This is the highest-emissions scenario in the CMIP5 climate projections ensemble, and is also the pathway that current emissions appear to be following (*69*). For this reason, and because we are interested in diagnosing the model response to rising GHGs, we utilize this scenario rather than the lower concentration pathways (RCP 2.6, 4.5, 6.0). Detailed information on the prescribed forcings for the historical and RCP 8.5 experiments may be found at `http://cmip-pcmdi.llnl.gov/cmip5/forcing.html`.

For our analyses, we used 23 of the available climate models in the CMIP5 ensemble to ensure comprehensive but relatively equal representation across different climate modeling groups. Where multiple ensemble runs were available, we used the first ensemble run. Table S3 lists the individual models and their resolution.

3.2. Analyses

We used precipitation (pr), 700 mb vertical velocity (wap) and skin temperature (ts) data from each of the 23 models to conduct our analyses. We chose to work with skin temperature over the ocean as opposed to SST due to difficulties analyzing SST data on various ocean native grids; skin temperature is effectively equivalent to SST in tropical regions. As not all individual model runs were conducted for the exact same period of time, we considered only data during the common shared periods of 1861–2004 (for the historical experiment) and 2006–2099 (for the RCP8.5 experiment). In all analyses, a time series of "Horn of Africa precipitation" refers to an area-average across 0–12°N, 40–55°E.

We recognize that it is important to consider the effect of increasing potential evapotranspiration (PET), associated with higher temperatures, on aridity in the Horn of Africa region. However, previous analyses of the contribution of PET to future projections of global drought in the CMIP5 ensemble determined that the predictions for the Horn region are dominated by changes in precipitation (*70*), hence we restrict our analyses to precipitation. Similarly, an experiment using a regional climate model demonstrated that although PET makes a contribution towards

more arid conditions, the simulated changes in rainfall dominate the trends in aridity for this particular region of Africa *(37)*.

To determine the multi-model mean trends in precipitation, we calculated the trend in each model respectively in units of percent change per year (which normalizes for inter-model differences in mean precipitation rates), regridded the data to a common resolution of 1° by 1°, then calculated the mean. We carried out this analysis on the annual mean, the two rainy seasons (MAM and SON), and the summer dry season for both the historical and RCP8.5 experiments with the same set of 23 models, to match our analysis of observational trends (Figure 2a in the main text). Analyses of the transitional DJF season did not yield notable patterns in either the observational or model data, so this season is omitted from our plots. Areas where at least 90% (21/23) of the models agree on the sign of change are stippled.

Figure S7 shows the multi-model mean results for precipitation trends in the historical experiment, on the same scale as the observational and RCP8.5 analyses shown in Figure 2. The patterns of change during the dry (JJA) and short rains (SON) seasons somewhat resemble the observational data (Fig. 2a), although the magnitude of change is muted in the model runs. During the long rains (MAM), the multi-model mean shows increasingly wet conditions, in disagreement with the observations. Increased rainfall during MAM and SON result in a slight moistening trend in the annual mean (Fig. S7). For all seasons, model agreement is low (median = 57% for Annual, JJA, and SON seasons; 61% for the MAM season).

To investigate the relationship between projected changes in Horn of Africa precipitation in the RCP8.5 experiment and surface temperature gradients across the Indo-Pacific, we created scatter plots of the percent change in average Horn of Africa precipitation vs. the change in Indian and Pacific Ocean zonal gradients for each model (Fig. S8). The Indian Ocean zonal gradient is defined as the difference between average surface temperatures in 0–15°N, 55-70°E and 5–10°S, 85–105°E. The Pacific Ocean zonal gradient is defined as the difference between average surface temperatures in 5°S–5°N, 85–130°W and 0–10°N, 130–170°E. Changes across the 21^{st} century simulation are calculated as the difference between average conditions from 2079–2099 and 2006–2026. Figure S8 shows scatter plots for the annual mean and each of the three main seasons, demonstrating that the relationship between the Indian Ocean gradient and precipitation is strongest during the short rains season (SON) and that there is no significant relationship between precipitation and the Pacific Ocean gradient in any of the seasons.

Previous work suggests that CMIP3 and CMIP5 models overestimate SST variability associated with the Indian Ocean Dipole (IOD), and that this may affect future projections of climate in regions affected by the IOD *(26)*. As discussed here, changes in the Indian Ocean SST gradient and IOD variability have a strong influence on Horn of Africa rainfall during the short rains season in the models. Hence, one would expect that the strength of IOD variability may impact the models' ability to simulate the seasonal cycle in precipitation as well as future projections.

We find that across the 23 models investigated here, there is no significant relationship between the strength of the IOD in the model and its ability to simulate the seasonal cycle in precipitation (Fig. S9). We do, however, find that models with a stronger IOD have a tendency to predict a greater increase in mean annual rainfall in the RCP8.5 experiment (Fig. S10), with maximum expression during the SON season (not shown). This suggests that an overly-strong interannual IOD in models exacerbates the dominance of the short rains changes in the future projections, even if it is not the sole cause for the poor simulation of the annual cycle.

Table S1. ^{210}Pb dates on P178-15 BC1. These data were collected via gamma counting at Woods Hole Oceanographic Institution.

Depth (cm)	^{210}Pb (Bq/g)	Error (1σ)	Median $^{210}Pb_{ex}$	Median Age	Error (1σ)
0.25	0.227	0.008	0.197	2000	0
0.75	0.216	0.010	0.186	1997	1
1.75	0.179	0.005	0.149	1991	2
2.75	0.163	0.005	0.133	1986	4
3.25	0.105	0.011	0.075	N/A	N/A
3.75	0.121	0.007	0.091	N/A	N/A
4.25	0.136	0.008	0.106	1977	6
4.75	0.160	0.007	0.129	N/A	N/A
5.5	0.143	0.010	0.112	N/A	N/A
6.5	0.110	0.006	0.079	1964	9
8.5	0.086	0.008	0.056	1953	11
10.5	0.061	0.005	0.030	1942	14
12.5	0.056	0.007	0.025	1931	17
14.5	0.046	0.010	0.016	1919	19
16.5	0.029	0.006	0	N/A	N/A
26.5	0.032	0.009	0	N/A	N/A

Table S2. Radiocarbon dates on P178-15 BC1. These data were collected and analyzed at the National Ocean Sciences Accelerator Mass Spectrometry Facility at Woods Hole Oceanographic Institution (OS). Also listed are the OxCal calibrated median ages (year AD), using the ^{210}Pb data as additional constraints.

ID #	Depth (cm)	Fm	Fm Error	^{14}C Age	Error (1σ)	Age (AD)	Error (1σ)
OS-101661	15.5	0.9167	0.0026	700	25	1890	11
OS-110256	20.5	0.9054	0.0025	800	25	1835	17
OS-110257	25.5	0.8984	0.0024	860	20	1781	23
OS-101815	30.5	0.8947	0.0025	895	20	1726	27
OS-110258	35.5	0.8854	0.0021	975	20	1674	30
OS-101816	40.5	0.8824	0.0022	1000	20	1628	35

Table S3. Radiocarbon dates on P178-15P. These data were collected and analyzed at the National Ocean Sciences Accelerator Mass Spectrometry Facility at Woods Hole Oceanographic Institution (OS) and Lawrence Livermore National Laboratory (LL). Also listed are the OxCal median calibrated ages (yr BP).

ID #	Depth (cm)	Fm	Fm Error	^{14}C Age	Error (1σ)	Age (BP)	Error (1σ)
LL-152757	5.5	0.9428	0.0033	475	30	<0	N/A
OS-101647	10.5	0.9119	0.0028	740	25	95	46
OS-101648	20.5	0.8797	0.0027	1030	25	368	42
OS-101649	30.5	0.8501	0.0024	1300	20	575	31
LL-152758	41.5	0.8228	0.0030	1565	30	731	36
OS-101650	50.5	0.8322	0.0025	1480	25	782	41
OS-101651	60.5	0.8144	0.0023	1650	25	914	37
OS-101652	70.5	0.7951	0.0027	1840	25	1121	45
OS-101654	80.5	0.7594	0.0025	2210	25	1452	46
LL-152759	90.5	0.7358	0.0026	2465	30	1709	50
OS-101655	110.5	0.7243	0.0023	2590	25	1931	45
OS-101657	130.5	0.6959	0.0022	2910	25	2308	43
OS-110259	145.5	0.6753	0.0018	3150	20	2656	49
LL-152760	150.5	0.6857	0.0028	3030	35	N/A	N/A
OS-101658	160.5	0.6413	0.0025	3570	30	3090	59
OS-101660	181.5	0.6100	0.0033	3970	45	3596	65
LL-152761	200.5	0.5787	0.0020	4395	30	4140	61
LL-156467	220.5	0.5524	0.0021	4765	35	4643	69
LL-152762	260.5	0.5052	0.0018	5485	30	5546	44
LL-156468	340.5	0.4295	0.0016	6790	35	7051	64
LL-152763	420.5	0.3092	0.0012	9430	35	9831	88
LL-156469	460.5	0.2863	0.0013	10045	40	10687	80
LL-152764	520.5	0.2322	0.0011	11730	40	12883	77
LL-156470	560.5	0.2005	0.0011	12910	45	14165	141
LL-159387	580.5	0.1715	0.0008	14160	40	16187	90
LL-156471	600.5	0.1476	0.0011	15370	70	17767	102
LL-152765	640.5	0.1271	0.0008	16570	60	19241	119
LL-159388	680.5	0.0718	0.0006	21150	70	24548	154
LL-156472	700.5	0.0559	0.0011	23160	160	26504	201
LL-156473	780.5	0.0340	0.0011	27170	260	30635	240
LL-156474	840.5	0.0264	0.0011	29180	340	33264	284
LL-152766	900.5	0.0129	0.0007	34930	450	37001	385

Table S4. List of the CMIP5 models used for the analyses. Both historical and future (RCP 8.5) climate experiments were studied. As only atmospheric variables were used, the listed resolution is for the atmospheric component of each model.

#	Model Name	Institution	Country	Resolution (Lat × Lon)
1	ACCESS 1.3	Commonwealth Scientific and Industrial Research Organisation and BOM	Australia	1.25°× 1.875°
2	BCC CSM1.1	Beijing Climate Center, China Meteorological Administration	China	2.8°× 2.8°
3	BNU ESM	Beijing Normal University	China	2.8°× 2.8°
4	CanESM2	Canadian Centre for Climate Modelling and Analysis	Canada	2.8°× 2.8°
5	CCSM4	National Center for Atmospheric Research	USA	1°× 1.25°
6	CESM1-CAM5	National Center for Atmospheric Research	USA	1°× 1.25°
7	CMCC-CESM	Centro Euro-Mediterraneo per I Cambiamenti Climatici	Italy	3.75°× 3.75°
8	CNRM-CM5	Centre National de Recherches Meteorologiques	France	1.4°× 1.4°
9	CSIRO Mk3.6	Commonwealth Scientific and Industrial Research Organisation	Australia	1.8°× 1.875°
10	FGOALS-g2	LASG, Chinese Academy of Sciences	China	2.8°× 2.8°
11	FIO-ESM	First Institute of Oceanography	China	2.8°× 2.8°
12	GFDL CM3	NOAA Geophysical Fluid Dynamics Laboratory	USA	2°× 2.5°
13	GFDL-ESM2G	NOAA Geophysical Fluid Dynamics Laboratory	USA	2°× 2.5°
14	GISS-E2-H	NASA Goddard Institute for Space Studies	USA	2°× 2.5°
15	GISS-E2-R	NASA Goddard Institute for Space Studies	USA	2°× 2.5°
16	HadGEM2-ES	Met Office Hadley Centre	UK	1.25°× 1.875°
17	INMCM4	Institute for Numerical Mathematics, Russian Academy of Sciences	Russia	2.5°× 2°
18	IPSL-CM5A-MR	Institut Pierre-Simon Laplace	France	1.2°× 2.5°
19	MIROC-ESM	Japan Agency for Marine-Earth Science and Technology, University of Tokyo	Japan	2.8°× 2.8°
20	MIROC5	Japan Agency for Marine-Earth Science and Technology, University of Tokyo	Japan	2.8°× 2.8°
21	MPI-ESM-MR	Max Planck Institute for Meteorology	Germany	1.8°× 1.875°
22	MRI-ESM1	Meteorological Research Institute	Japan	1.1°× 1.125°
23	NorESM1-M	Norwegian Climate Centre	Norway	1.9°× 2.5°

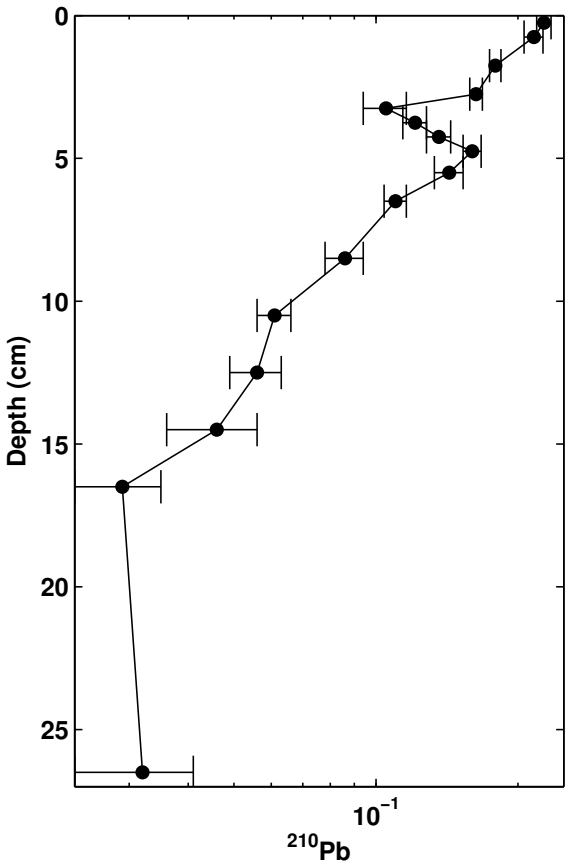

Figure S1. ^{210}Pb data from P178-15 BC1. Error bars represent the 1σ uncertainty.

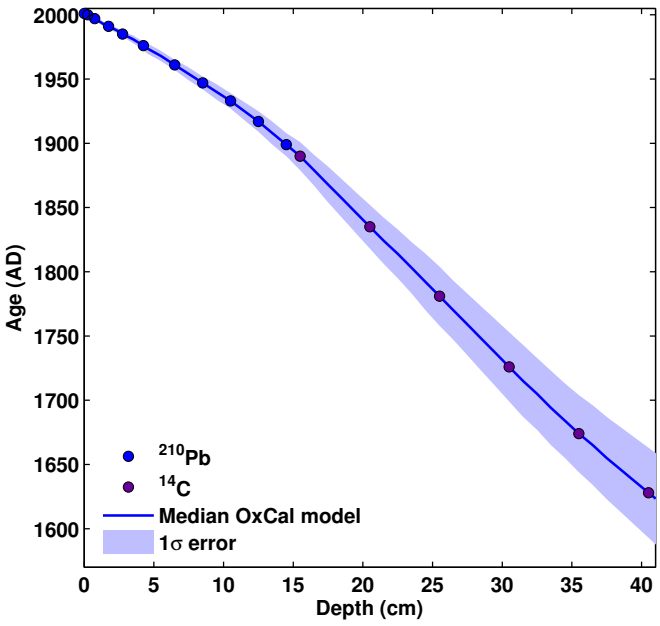

Figure S2. The age model for P178-15 BC1.

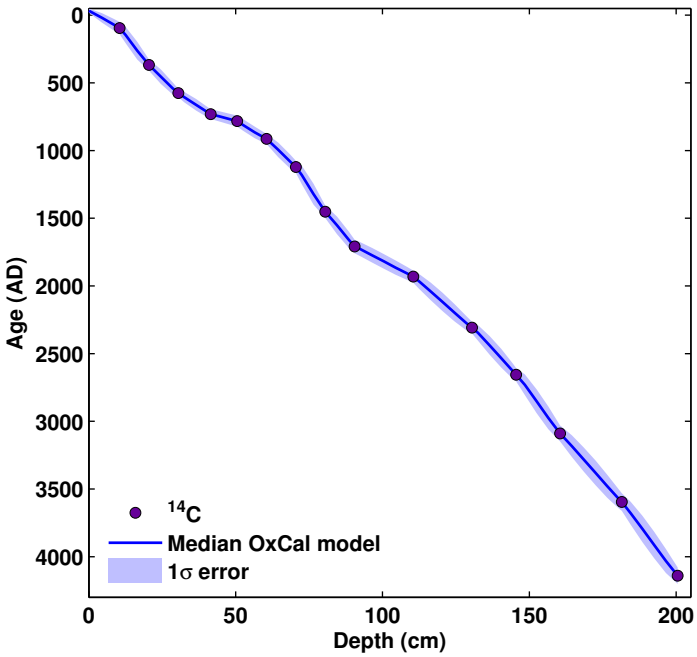

Figure S3. The age model for P178-15P for the last 4000 years.

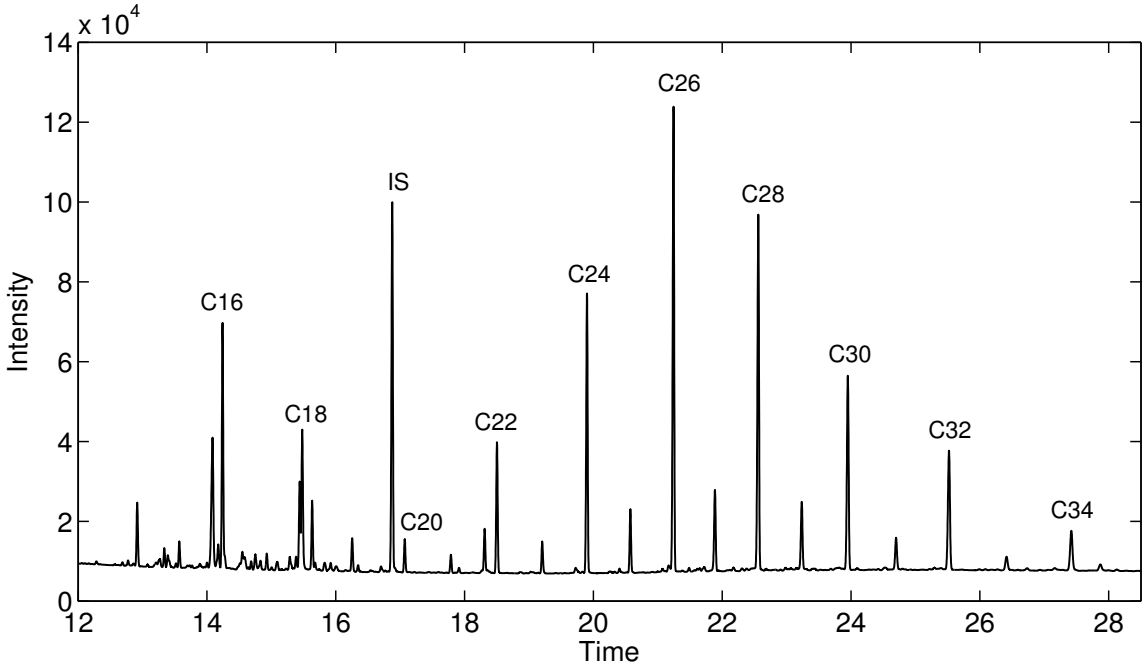

Figure S4. A sample GC-FID chromatogram of fatty acids (as methyl esters) from core P178-15P. Clear even-over-odd preference indicates a source derived primarily from higher plants. Labels denote the acids with even-numbered chain lengths. The C_{30} acid was targeted for δD_{wax} analyses.

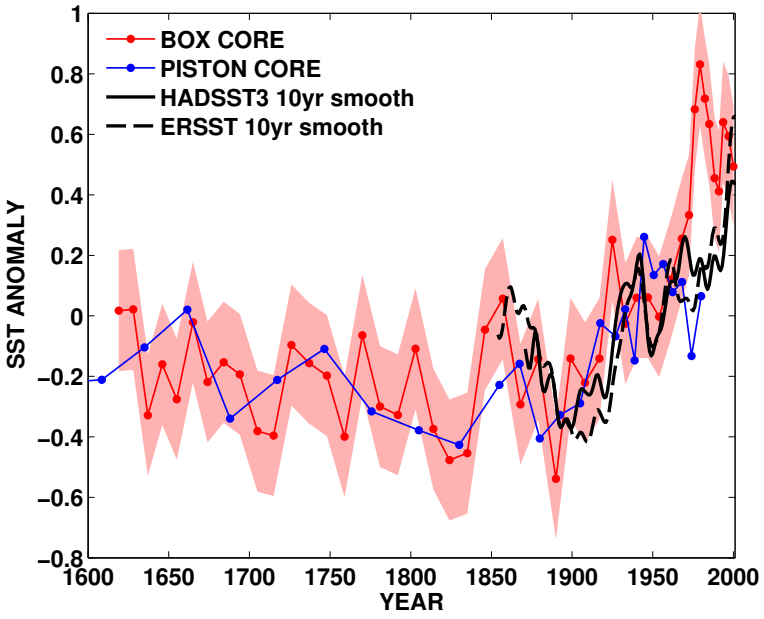

Figure S5. TEX_{86}-based SST anomalies from P178-15 BC1 (box core) vs. instrumental observations. The instrumental observations are the 10-year smoothed SST anomalies from the grid point nearest to the Gulf of Aden site (HadSST3 (*71*, *72*) and ERSSTv3b (*73*)). Piston core data are overlaid in blue for comparison; the data generally agree with the box core.

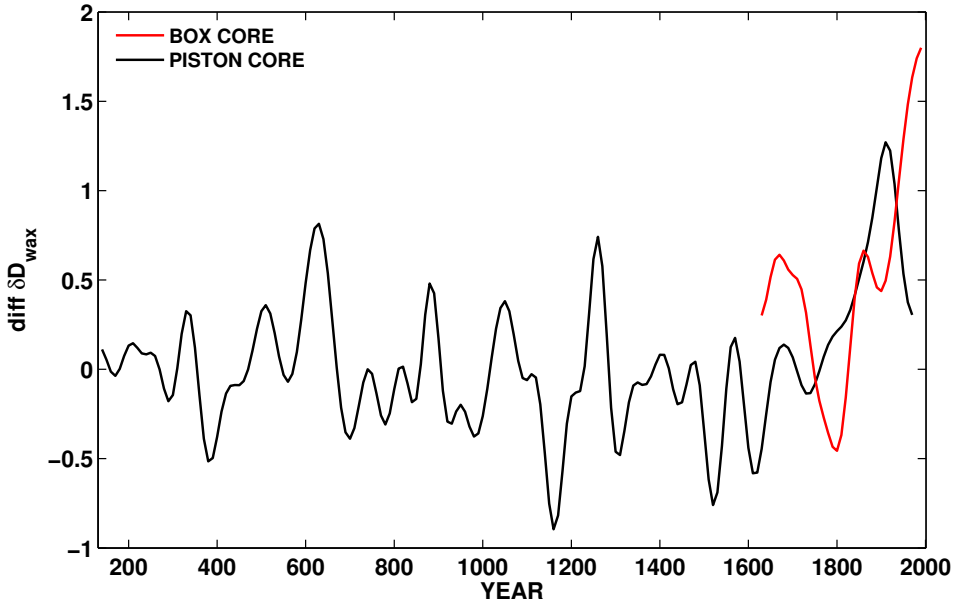

Figure S6. First derivative of the δD_{wax} data from the Gulf of Aden. The data were resampled to a common time interval (10 yr), then smoothed with a 10-pt (100 yr) Gaussian smoothing filter prior to calculation of the first derivative.

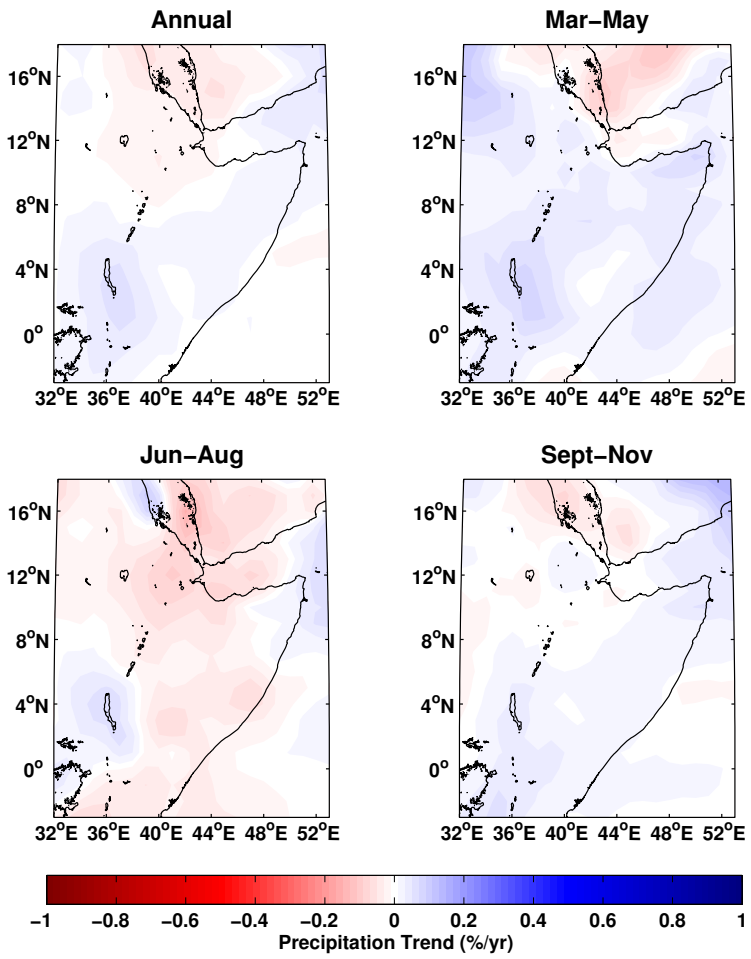

Figure S7. Multimodel mean of trends in simulated precipitation from CMIP5 historical experiment. In all cases, model agreement is below 90%, hence no stippling is shown.

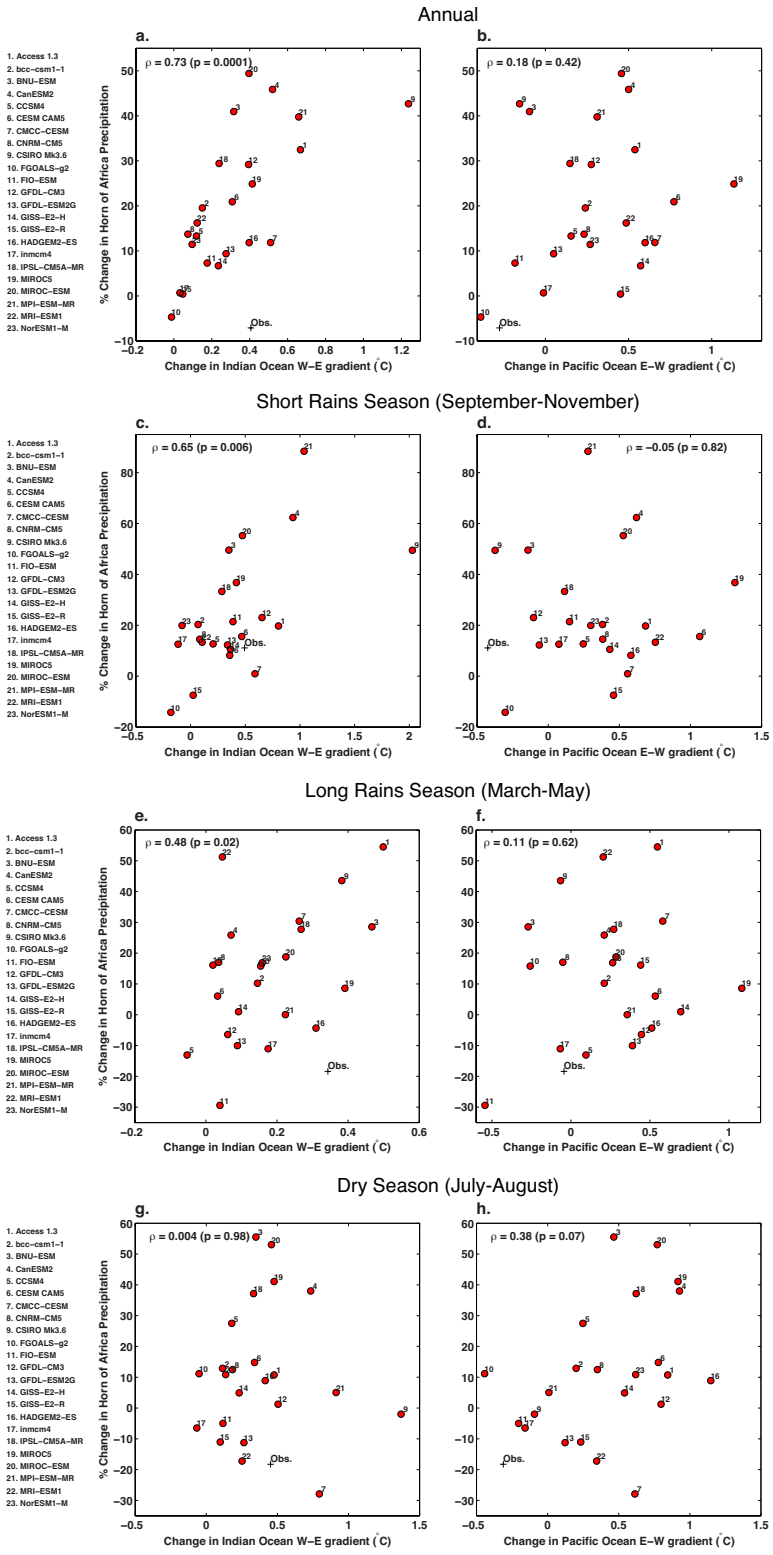

Figure S8. Projected change (%) in Horn of Africa precipitation versus projected changes in zonal surface temperature gradients in the Indian and Pacific Ocean basins. Both annual and seasonal relationships are shown. Observational values, calculated from the HadiSST and GPCCv6 products, are plotted for comparison (black crosses).

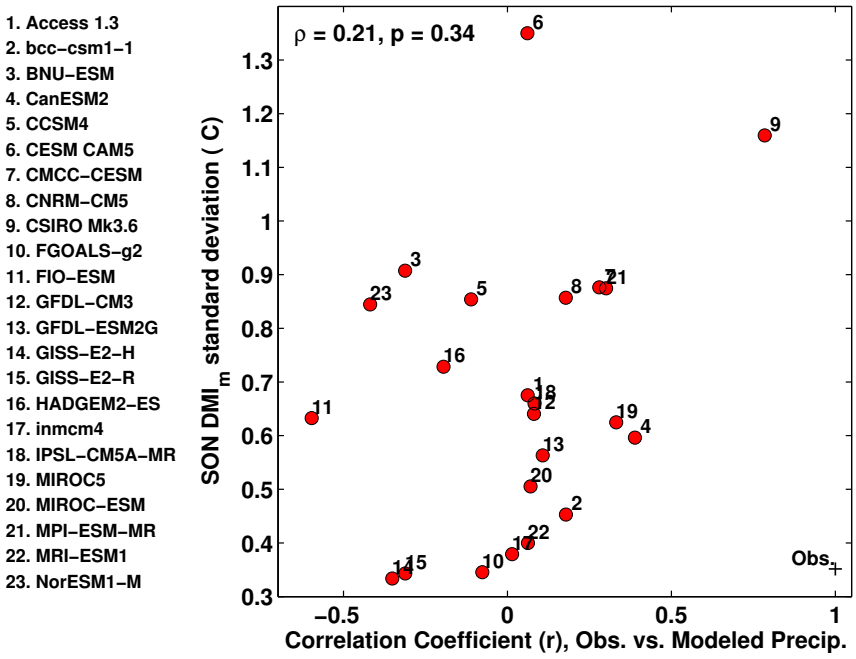

Figure S9. Scatterplot of the correlation coefficient between the simulated annual cycle of precipitation in the Horn of Africa vs. the observed annual cycle (from GPCC v6) and the standard deviation of a modified Dipole Mode Index (DMI_m). DMI_m represents the strength of the Indian Ocean Dipole in each model and is calculated as the difference between average surface temperatures across 0–15°N, 55-70°E and 5–10°S, 85–105°E, differing only slightly from the standard DMI gridboxes (*74*) in order to avoid land areas in the *ts* field. These gridboxes are the same as the ones we use to calculate zonal gradients in the RCP 8.5 scenario (Fig. S8). Observed values (correlation is by definition 1, SON DMI_m = 0.35, using HadiSST) are shown for comparison. Spearman correlation (ρ) and significance are shown at the top of the plot.

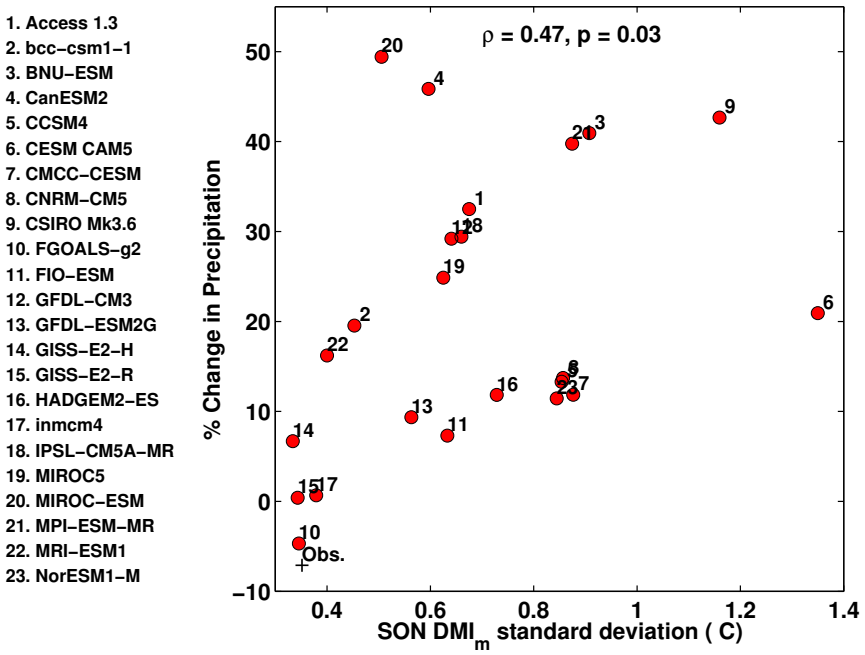

Figure S10. Scatterplot of the SD of a modified Dipole Mode Index (DMI_m) and the projected change in precipitation for the RCP 8.5 experiment. Observed values for the 20th century (based on HadiSST and GPCCv6 precipitation) are shown for comparison. Spearman correlation (ρ) and significance are shown at the top of the plot.